Architected Polymer Foams via Direct Bubble Writing

Claas Willem Visser[1‡*], Dahlia N. Amato[1,2], Jochen Mueller[1], and Jennifer A. Lewis[1,*]

[1]Wyss Institute for Biologically Inspired Engineering and John A. Paulson School of Engineering and Applied Sciences, Harvard University, Cambridge, MA 02138, USA

[2]School of Polymer Science and Engineering, University of Southern Mississippi, Hattiesburg, Mississippi 39406, USA

‡Now at: Engineering Fluid Dynamics group, Thermal and Fluid Engineering Department, Faculty of Engineering Technology, University of Twente, Drienerlolaan 5, 7500AE Enschede.

*Corresponding authors: C.W. Visser (c.visser@utwente.nl) and J.A. Lewis (jalewis@seas.harvard.edu)

Keywords: 3D printing, foams, functionally graded materials, multifunctional materials, polymers

Polymer foams are cellular solids composed of solid and gas phases that are widely used as personal protection gear,[1] pressure sensors,[2] thermal insulation,[3] acoustic materials,[4] and even scaffolds for artificial tissues[5]. Their mechanical, thermal, and acoustic properties are determined by the respective composition, volume fraction and connectivity of both phases.[6,7] Open-cell foams consist of a continuous gas phase with intervening solid struts. These foams are mechanically weak, yet highly flexible when compared to closed-cell foams, and simultaneously allow liquid or gas to readily flow through their interconnected open cells. By contrast, closed-cell polymer foams possess discrete bubbles that are surrounded by solid cell walls. These foams exhibit enhanced load-bearing capabilities, yet their transport is limited.

Both open- and closed-cell polymer foams are typically produced by conventional processing methods that rely either on the *in situ* formation of bubbles via foaming agents,[8,9] decompression of liquid polymer resins that contain dissolved gas,[10,11] templating,[12,13] or mechanical frothing.[14,15] While large volumes of material can be generated using these methods, the resulting foams possess a broad distribution of cell (bubble) sizes owing to the stochastic nature of bubble nucleation and growth processes.[16] In addition, bubble drainage

and Ostwald ripening (gas transport from small to large cells) within the liquid foam prior to polymerization further broaden the bubble size distribution. To overcome this inhomogeneity, microfluidic techniques have recently been used to generate polymer foams composed of locally monodisperse bubbles[17,18] of controlled connectivity[19] or gradients.[20,21] However, it is difficult to scale up these techniques to create large production volumes and free-standing or spanning features are still out of reach. Additive manufacturing (AM) provides an alternative route for controlling the composition and architecture of polymer foams.[22] To date, direct ink writing,[23] stereolithography[24,25] and two-photon lithography[26] have been used to create porous polymer constructs with highly tunable properties. For example, architected polymer lattices have been produced in several geometries with dense,[27–30] hollow,[24,25,31,32] and foam-based [15,33,34] struts. In the latter case, however, there was limited control over the bubble size and distribution within each strut, since those lattices were produced via direct foam writing.[15,34,35] Integrating additive manufacturing with liquid[36] or solid[37,38] templating enabled fabrication of hierarchical architectures, but simultaneously optimizing the precision, flexibility, and throughput of these multi-step processes is prohibitively challenging. Therefore, new methods are needed that enable foam architectures to be systematically patterned across multiple scales within a single construct,[39,40] since even simple functionally graded materials may offer major benefits for applications ranging from impact absorbers[41] to micro-filters[42].

Here, we report a new high-throughput additive manufacturing method, referred to as direct bubble writing, for creating polymer foams with locally programmed bubble size, volume fraction and connectivity. Direct bubble writing relies on rapid generation and patterning of liquid shell-gas core droplets produced using a core-shell nozzle, as shown in **Figure 1**a,b and **Movie 1**.[43] These polymer foams are able to retain their overall shape, since the outer shell of these bubble droplets consist of a low-viscosity monomer that is rapidly polymerized during the printing process.[44] The transition between open- and closed-cell foams is independently controlled by the gas used, i.e., use of an oxygen-rich gas suppresses polymerization leading to open cell foams, whereas closed-cell foams are generated using

oxygen-deficient gases. The relative density of the resulting solid ($\rho_{rel} = \rho/\rho_s$, with ρ being the construct density and ρ_s the polymer density) can be tailored *on-the-fly* by adjusting the gas pressure used to produce the bubble droplets. When the gas pressure is zero, solid polymers ($\rho_{rel} = 1$) are produced. As the gas pressure increases, polymer foams are produced. By mounting our core-shell printhead onto a 3-axis robotic stage, we can programmably define the macroscopic shape as well as the local microstructure and functional properties of pure polymer and composite foams.

Direct bubble writing relies on the controlled ejection of a train of bubbles from the core-shell nozzle (shown in Figure 1c-g) that travel to the substrate. To assess the bubble ejection dynamics, we systematically varied the gas pressure P and the flow rate Q applied to these nozzles (Figure 1h-k and **Movie 2**). At low gas pressures, pure-liquid dripping is observed for low flow rates $Q < 5 \pm 1$ ml min^{-1}, followed by pure-liquid jetting at higher flow rates (Figure 1h). This transition occurs if the inertia of the liquid exceeds surface tension forces at the nozzle tip, as described [1] by a Weber number $\mathrm{We} = \rho_l D_o \frac{V_l^2}{\sigma_l} > 4$, with inner nozzle diameter $D_o = 0.44$ mm, liquid density $\rho_l = 1.09 \cdot 10^3\ \mathrm{kg\,m^{-3}}$, surface tension $\sigma_l = 23.5\ \mathrm{mN\,m^{-1}}$, and liquid velocity $V_l = 4Q/(\pi D_o^2)$. This threshold corresponds to $Q = 4.7$ ml min^{-1} as indicated by the dashed line in Figure 1l, which is consistent with our measurements.

Increasing the pressure in the jetting regime results in ejection of a train of bubbles either in the monodisperse regime (Figure 1i) or a bi- or tridisperse regime (Figure 1j). We hypothesize that the transition from liquid jetting to bubble ejection occurs if the gas pressure exceeds the total liquid-induced pressure $P_{tot} = P_I + P_\mu + P_\sigma$ at the inner nozzle tip. Here, the Bernoulli equation $P_I \sim \rho_l V_l^2$ accounts for the hydrodynamic pressure increase at the stagnation point of the gas-liquid interface (indicated by the black dot in Figure 1e). The Darcy-Weisbach equation $P_\mu \sim \frac{128\mu_l Q L}{\pi D_o}$, with viscosity $\mu_l = 9.5\ \mathrm{mPa\,s}$, describes the viscous pressure build-up for pipe flow, in this case over the distance $L = 0.6$ mm between the outer and inner nozzle tips. The Young-Laplace equation $P_\sigma = 4\gamma_l/D_i$ describes the pressure required to punch

through the liquid-air surface at the inner nozzle tip with diameter $D_i = 0.3\ \mathrm{mm}$. All three partial pressures are of order $\mathcal{O}(1)\ \mathrm{kPa}$ in the studied regime and therefore cannot be ignored. For the inertial and the viscous terms, scaling relations (~) are used since the nozzle geometry and the gas flow may affect the liquid velocity. Figure 1l shows that the transition from gas-free jetting to bubble ejection is well-described by $P = cP_{tot}$, with dimensionless prefactor $c = 0.82$. In view of the major simplifications made, this prefactor is remarkably close to 1. At high gas pressures $P \gg P_{tot}$, a spray of droplets with poorly defined sizes and trajectories is produced (Figure 1k), which is not suitable for direct bubble writing.

Combined, these results suggest that $\frac{P}{P_{tot}} \gtrsim 0.82$ and $We \gtrsim 4$ are necessary constraints for bubble train ejection from core-shell nozzles. These dimensionless parameters readily translate into the minimum liquid flow rate and gas pressure for bubble ejection as a function of the liquid properties and nozzle size. An additional constraint is that spraying should be prevented, but modeling this more complex [2] transition is beyond the scope of the current work. Here, we selected a flow rate $Q = 10$ mL min^{-1} for all experiments, because it allows for controlled bubble ejection over a wide range of gas pressures. Note, this flow rate is more than two orders of magnitude higher than those used for generating polymer foams within microfluidic devices.[3] At this flow rate, we created a representative 3D polymer foam printed in the monodisperse bubble regime (Figure 1m-o), which demonstrates that the cell (bubble) size is well controlled.

Direct bubble writing can be used to create both open- and closed-cell polymer foams simply by switching between air and nitrogen gas, respectively. When air is used, oxygen diffuses into the liquid cell walls (outer shell) inhibiting polymerization of the acrylate-based ink. The oxygen penetration depth is estimated as $\delta = (Dt_S)^{\frac{1}{2}} \approx 20$ µm, where $D \approx 2 \cdot 10^{-9}$ m^{2}s^{-1} denotes the oxygen diffusion coefficient, [47] and $t_S \approx 200$ ms refers to the characteristic polymerization time estimated from high-speed imaging (**Movie 3**). Since the liquid interfaces between adjacent cells are less than 40 µm thick (**Figure S1**), oxygen will

inhibit polymerization, eventually leading to rupture of the liquid cell wall.[48] By contrast, the thickness of the struts is roughly 100 μm or higher. Hence, while a surface layer is oxygen-inhibited, their core polymerizes into a solid skeleton that constitutes the desired open-cell foams (**Figure 2**a and **Movie 4**). When oxygen is replaced by nitrogen gas, even the thin liquid interfaces between adjacent cells polymerize upon exposure to UV light, resulting in closed-cell polymer foams (Figure 2b and **Movie 5**). The transition between open-cell and closed-cell foams is maintained over the full density range (see Figure S1).

Micro-computed tomography (micro-CT) is used to obtain 3D scans of representative open- and closed-cell polymer foams (**Figure S2**). The resulting image stacks are converted into black and white images (Figure S2a-c), followed by advanced processing to determine their effective diameter (Figure S2d-h and Extended Methods). This procedure is sufficiently robust for processing both open- and closed cell foams (Figure S2i-p). The polymer foam density decreases from that of nearly 100% solid at low pressures ($\rho_F = 1100$ kg m^{-3} at $P \leq$ 1.9 kPa) to a 10% solid at high pressures ($\rho_F = 115$ kg m^{-3} at 4.4 kPa), as shown in Figure 2c. At low pressures ($2.1 \leq P \leq 2.6$ kPa), monodisperse bubbles result in polymer foams with a uniform cell size and a quasi-crystalline packing (Figure 2d and Figure S2m). Bidisperse polymer foams are observed for $2.8 \leq P \leq 3.4$ kPa. In these foams, bubbles with two characteristic diameters of 0.3 ± 0.1 and 0.7 ± 0.1 mm (Figure 2e-g and Figure S2n) are observed. The cell size distribution is plotted in Figure 2f, which reveals that the characteristic bubble diameter (with a coefficient of variation of 4%) could be tuned from 0.4 to 0.7 mm (Figure 2g). Finally, at even higher gas pressures, polymer foams with a tri-disperse distribution are observed at P = 3.6 kPa (Figure S2o), followed by a broad cell size distribution at P = 4.8 kPa (Figure S2p).

Polymer foams with programmed shape and hierarchical porosity can be manufactured by direct bubble writing while translating the printhead in x-, y-, and z-directions as bubbles are continuously ejected. For printing speeds of $V > 20$ mm s^{-1}, continuous filaments are formed (**Figure 3**a). The filament width increases with increasing pressure or

decreasing print speed (Figure 3b). Since the printed filaments rapidly solidify, they can be readily stacked to produce 3D architectures. As one example, we created a 3D triangular lattice with outer dimensions of 60x40x3 cm^3 (Figure 3c-f), which was printed in 22 minutes at a liquid flow rate of 10 mL min^{-1} (note: the total flowrate increases to ~ 80 mL min^{-1} through the entrainment of air). Vertical pillars of controlled height can be fabricated by immobilizing the printhead for a fixed duration (**Figure S3**a-b). By moving the printhead at low speed in-plane ($V < 14$ mm s^{-1}), one can control the inclination angle of each pillar (Figure S3c), which could be generated up to 40° for low-density materials (Figure S3d; see Materials and Methods for further details). Bridges between pillars could be formed by touching pillar tips out-of-plane (Figure S3e). The transition between inclined pillars to filaments occurs at $V = 15 \pm 0.5$ mm s^{-1}, at which horizontal spanning features form. We take advantage of this capability to create 3D woodpile architectures that possess interconnected channels both between and within the spanning foam features (Figure S3f).[49]

Using direct bubble writing, we can also produce 3D polymer foams with locally graded mechanical properties (**Figure 4**). We can independently produce foams of low (soft) and high (stiff) stiffness (Figure 4a,b) that either compress or maintain their shape under a 100 g mass, respectively. We can integrate stiffness gradients within a given printed foam simply by locally varying the bubble density, which allows their stiffness to be tuned over several orders of magnitude (Figure 4c). Theory predicts a power-law dependence of normalized stiffness, $\frac{E}{E_0} \sim (\rho_{rel})^n$, on the relative density, $\rho_{rel} = \frac{\rho}{\rho_0}$, where ρ_0 and E_0 denote the bulk density and elasticity, respectively. Note, an exponent $n = 2$ is predicted and widely observed for open-cell solids, whereas $1 < n < 2$ is predicted for closed-cell solids with increasingly thin walls[6]. Although these values are derived for $\rho_{rel} < 0.1$, they are typically also accurate at higher densities for a wide range of cellular solids. We find that $n \approx 2$ for closed-cell polymer foams, which suggests that the outer surface does not strongly contribute to their overall stiffness, which is expected given their low thickness (Figure S1). By contrast, we observe $n \approx 4$ for open-cell polymer foams, which may arise due to their relatively thin struts.[50] The high values

of n indicate exceptional stiffness tunability over a moderate density range, which we exploited for conformal printing of a tri-stable cap with stiff and soft regions (Figure 4d). The printed cap snaps into different shapes upon continued compression from the top (Figure 4e), of which states (i), (iii), and (iv) are stable as reflected by the force-indentation curve shown in Figure 4f. Since local gradients in stiffness can be programmably defined at any location via direct bubble writing, this approach offers a pathway for creating 3D architected foams whose shape and mechanical response is specifically optimized for a given application.

As a final example, conductive composite foams were developed for use as pressure sensors. Specifically, we generated silver nanoparticles (NPs, **Figure 5**a) *in situ* within the printed polymer foam by UV-induced reduction of silver nitrate that was predissolved within the liquid resin ink.[51] The printed composite foams exhibit an elastic modulus comparable to their pure polymer foam counterparts (**Figure S4**a-b). The electric resistance of conductive composite foams of varying stiffness is measured under controlled compression, by placing each foam between two electrodes (Figure 5b). These data reveal that the electrical resistance decreases with increasing compressive stress and foam stiffness (Figure 5c). To assess their pressure sensing performance, the sensitivity $S = (\frac{dR}{R})/dP$ as a function of applied stress is shown in Figure 5d. The absolute sensitivity is comparable to recently developed foam-based pressure sensors (Figure S4d). The sensors maintain their elasticity under moderate compression and repeated cycling (**Figure S5**a,b). For example, the low-density ($\frac{\rho}{\rho_0}$ =0.18) samples exhibit elastic behavior up to 60% strain (Figure S5c) in the 0.2 to 20 kPa range with limited hysteresis as a function of the strain (Figure S5d) and stress (Figure S5e). High-density samples ($\frac{\rho}{\rho_0}$ =0.41) are elastic up to 40% strain and allow virtually hysteresis-free pressure measurements over a large stress range from 0.5 to 100 kPa. As such, direct bubble writing enables one-step fabrication of pressure sensors with controlled shape and tunable stiffness for a highly relevant stress range that includes both gentle touch (<10 kPa) and object manipulation (10 to 100 kPa).In summary, we report a new additive manufacturing method,

known as direct bubble writing, for creating polymer foams with programmable macroscopic shape and locally tunable microstructure and functional properties. A directed train of monomer-containing bubbles is ejected from a nozzle at rates exceeding 10 mL min^{-1} and printed onto a substrate, where the material is polymerized *in situ* by UV light. The gas pressure controls the local foam density, which enables the generation of polymer foams with varying Young's modulus $2\,\mathrm{kPa} < Y < 2\,\mathrm{MPa}$. Open- and closed-cell polymer foams are produced using air- and nitrogen- filled bubbles, respectively. Using direct bubble writing, we fabricated homogeneous and graded polymer foams in several motifs, including 3D lattices, shells, and out-of-plane pillars. Through the incorporation of silver nanoparticles, we produced conductive composite foams with controlled stiffness for use as soft pressure sensors. Direct bubble writing opens new avenues for rapidly designing and manufacturing designer polymer foams on demand.

Materials and methods

Materials: Polymer foams were created using an ink composed of polyethylene glycol-diacrylate (35wt%, PEG-DA, Mn = 700 Da, 35%wt, Sigma), photoinitiator (1 wt%, Irgacure 651, BASF), surfactant (2 wt%, Tween 80, Sigma), and deionized water (62%wt). First, PEG-DA, Tween 80 and Irgacure 651 were mixed together for 10 min at 2350 rpm using Flacktek speed mixer. Next, deionized water was added to this mixture, while continuously stirring for 30 sec. The resulting liquid resin was stored prior to use to prevent photopolymerization. Conductive polymer foams were prepared by creating a composite ink following the same procedure outlined above, except that silver nitrate (10 g) was added to the base mixture.[51] The inks were purged with nitrogen for 20 min prior to filling each syringe in an oxygen-free atmosphere. The viscosity of the ink was measured with an Ex2000 Rheometer (TA Instruments) and the surface tension was determined with the hanging drop method.

Direct bubble writing: A customized printhead was developed for direct bubble writing, which consists of a core-shell nozzle surrounded by four optical fibers. The printhead is mounted on a 3D-axis motion-controlled stage (Aerotech). Disposable core-shell nozzles were created using an Envisiontec Aureus printer. The nozzle inlets were connected to PEEK tubing using standard Luer-lok components (IDEX Health&Science). Inside each nozzle, liquid and gas channels are concentrically aligned. The inner and outer diameters of each nozzle are 0.30 ± 0.02 mm and 0.44 ± 0.02 mm, respectively. UV light is provided by an Omnicure light source (Omnicure S2000, Excelitas technologies) connected to a splitting optical fiber. The four ends of this optical fiber were pointed towards the location of bubble impact (~ 10 cm below the nozzle) to promote photopolymerization with a light intensity of 0.8 ± 0.2 mW cm^{-2} over a circular area (5 cm in diameter). Optical images of the printing process were obtained using a Q-click F-M12 camera (Qimaging) with shutter time of 30 µs. High-speed videos were obtained using a V7.1 (Phantom) camera operated at 6000 frames s^{-1}.

Open and closed polymer foams were printed in a layerwise build pattern at speed of 40 mm s^{-1} to 100 mm s^{-1} depending on the applied gas pressure. The center-to-center distance between adjacent features ranged between 4 to 7 mm. The nozzle height was held at 10 cm

above substrate and did not change during printing. Polymer foams in the shape of a spherical cap were printed conformally onto a mold. The object was manually removed from the mold after printing. Conductive polymer foams were printed and exposed to broadband UV light from both above and below for 10 min per side to enhance the formation of silver nanoparticles. After printing, the foams were slowly dried at 70% and 85% relative humidity. The foam mass and outer dimensions were measured before and after drying. They exhibited a mass loss of 59 ± 1% and linear shrinkages of 27.8 ± 1.1% in x-y direction and 28.0 ± 2.1% in z-direction. Upon drying, the foam density increased by 9%.

Vertical pillars were formed holding the printhead in a constant position both vertically and laterally. Inclined pillars were printed by moving the printhead laterally at $V < 10$ mm s^{-1}. V-shaped bridges were made by printing two inclined pillars from their base and connecting their tips. If the vertical pillar growth velocity v_z is independent of the printhead velocity V (which is valid in the low-V limit), $\theta = \arctan\frac{V}{v_z}$, where $\theta = 0$ represents a vertical pillar and $\theta = 90°$ represents a horizontal filament.[52] This model breaks down for $\theta > 20°$ for low pressures and $> 40°$ for all pressures, as the prescribed velocity $V = v_z \tan\theta$ is so high the vertical pillar growth velocity v_z is no longer constant. The vertical pillar growth velocity v_z was determined from a linear fit to the height versus time curves (Figure S3b).

Microstructual characterization: Printed polymer and composite foams were laser-cut into cuboid shapes of known dimensions and weighed to determine their relative density. Optical images of their top surface were taken after printing using an optical microscope (Zeiss Discovery.V20). Their characteristic bubble diameter was determined using image analysis carried out on at least 50 bubbles. The bubble size distribution is described by a Gaussian fit, $ae^{-\frac{(x-\mu)^2}{2\sigma^2}}$, where a denotes a fitting constant, μ the mean cell diameter, and σ the standard deviation. Since these optical measurements are based on the foam surface, we also determined the bubble size distribution using 3D micro-CT. Printed foams were cut to an approximate size of 1cm^3 and placed in a micro-CT scanner (X-tec, HMXST225). After CT-scanning and image reconstruction with standard software (VG StudioMax), an image stack was obtained for each sample. The images were converted to black-and-white, and the size of each 3D black cell that is surrounded by white pixels (cell walls) was determined by image processing in Matlab (see extended methods for additional details).

Mechanical testing: Polymer foams were laser-cut with a Universal Laser System PLS6.150D to sizes of ~15 mm x 15 mm with a thickness between 5 and 20 mm (note, thicker samples corresponded to foams with higher porosity). Each foam sample was placed in an Instron machine (Model # 5566) and their stress-strain behavior was measured under compressive loading conditions at a crossbar velocity of 0.1 mm s^{-1} to 1 mm s^{-1} with the higher velocity used for the thicker samples. Their Young's modulus was obtained by a first-order fit over the linear regime of the stress-strain curve.

Conductive polymer foams were tested by first attaching copper electrodes with a surface area of 20x20mm^2 to both sides of the Instron machine. These electrodes were connected to a computer-controlled resistance meter (Hioki M3544-01) that measured the electrical resistivity as a function of time. Their pressure sensitivity was determined by correlating the measured resistivity values to their stress-strain curves in Matlab.

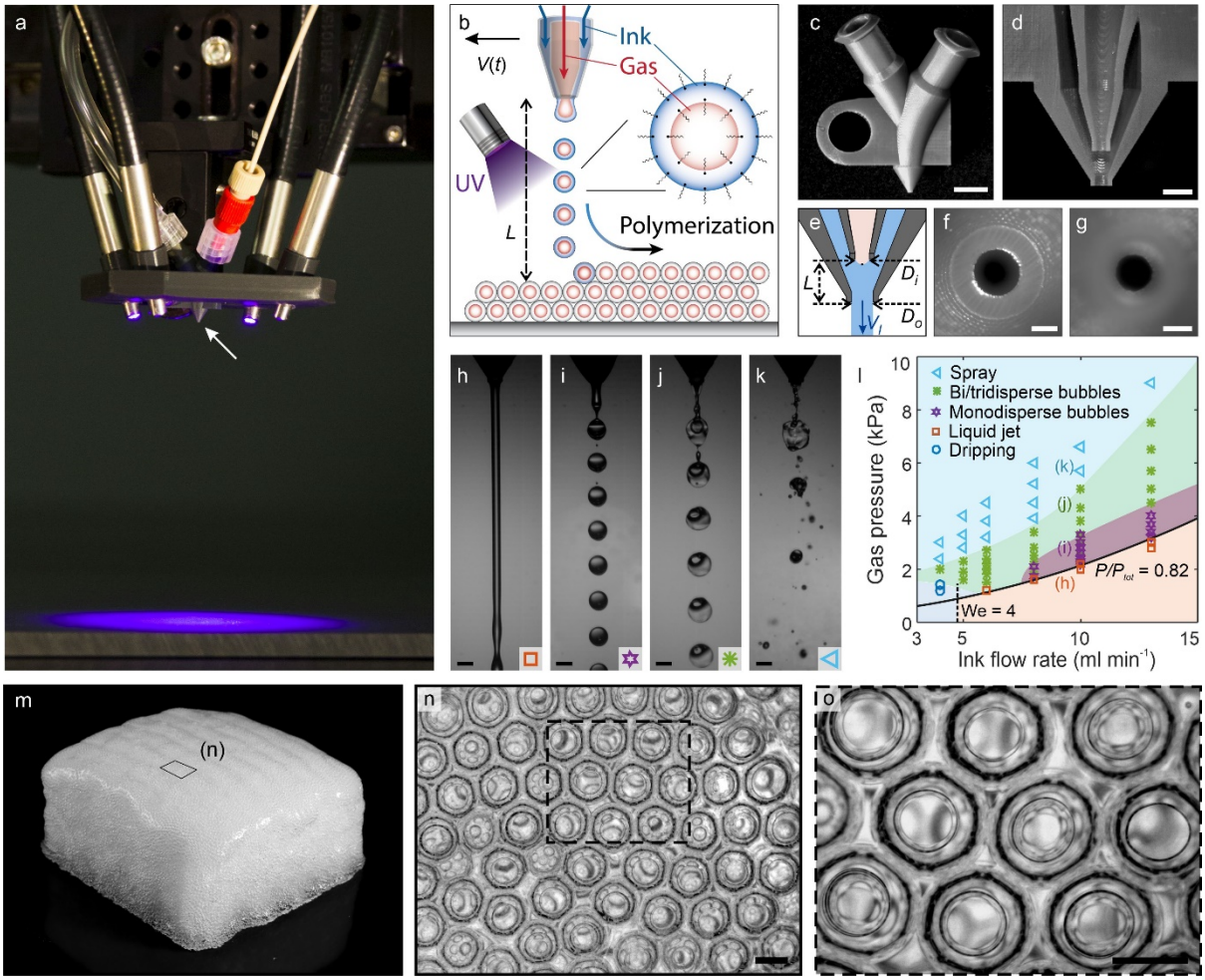

Figure 1: Direct bubble writing. (a) Optical image of the printhead, where the arrow indicates the nozzle tip. The transparent tubing (top-left) supplies the gas and the thin beige tubing supplies the liquid. Four optical fibers are locked in place by a separately printed holder, emitting UV light to the purple spot at the substrate.[53] (b) Schematic illustration of bubbles composed of a fluid shell-gas core, which are ejected from the core-shell nozzle onto the substrate and rapidly photopolymerized. Optical images of the (c) surface and (d) cross-section of the core-shell nozzle. (e) Scheme of the cross section. (f,g) Optical images of (f) the shell orifice and (g) the core orifice. (h) Ejection of a purely liquid jet occurs at low gas pressures. (i) Monodisperse and (j) bidisperse bubbles are ejected at intermediate gas pressures. (k) At higher gas pressures, the bubbles burst upon ejection and directionality is lost. (l) Phase diagram delineating each bubble ejection regime as a function of the fluid (ink) flow rate and gas pressures used. The markers correspond to h-k. The solid line indicates the modeled transition from pure-liquid ejection to bubble ejection at $P/P_{tot} = 0.82$ and the dashed line indicates the modeled transition from dripping to jetting at We = 4. The background colors serve as a guide to the eye. (m-o) Optical image of a printed polymer foam (70 x 70 x 35 mm^3) fabricated by direct bubble writing at a pressure of 2.4 kPa. (n,o) Optical images of cells at the top surface. Scale bars: (c) 5 mm, (d,e) 1 mm, (f,g) 0.25 mm, (n,o) 0.5mm.

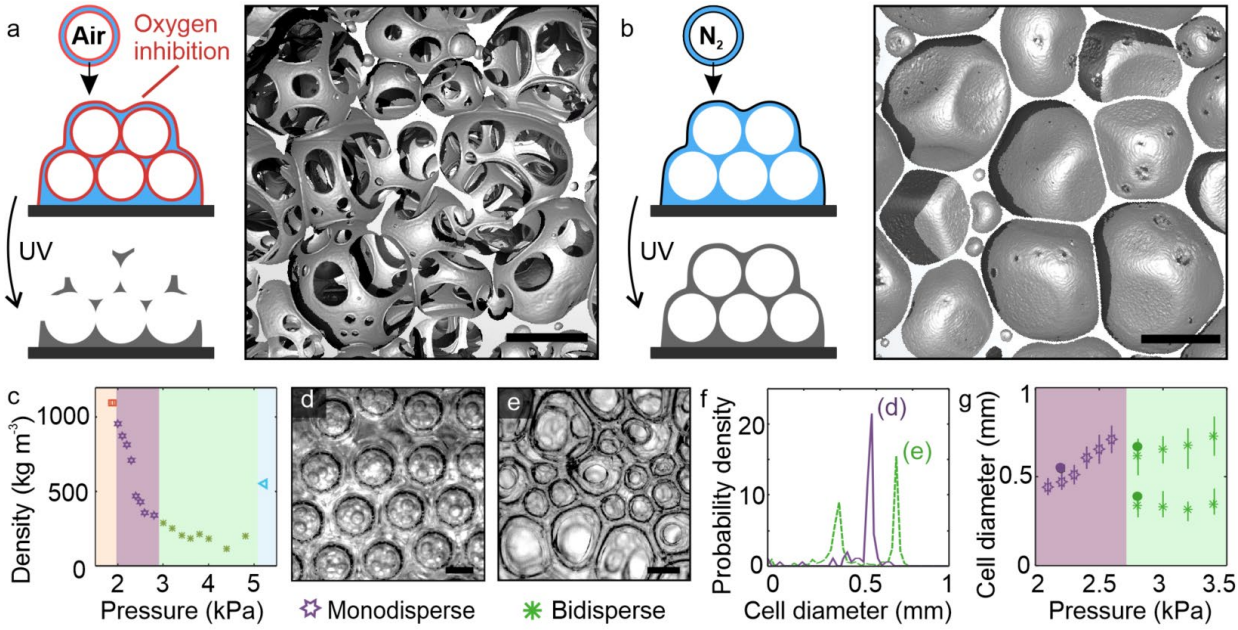

Figure 2: Open- and closed-cell polymer foams. (a) Open-cell polymer foams are formed by printing air-filled bubbles. (b) Closed-cell solids are formed by printing nitrogen-filled bubbles, resulting in polymerization of the intact cell walls. The examples in (a,b) show micro-CT scans of polymer foams with similar densities of ρ = 131 ± 5 kg m^{-3} and ρ = 122 ± 5 kg m^{-3}, respectively. (c) The density as a function of the pressure applied to the nozzle; colors and markers correspond to Figure 1l. (d) Monodisperse polymer foams are formed by direct bubble writing at low pressures (shown: P = 2.2 kPa), whereas (e) a bidisperse size distribution is observed (i.e. two dominant cell sizes) for intermediate pressures (shown: P = 2.8 kPa). (f) Cell size distributions corresponding to (d,e). (g) Cell size distribution as a function of the pressure, as determined with optical microscopy (open markers) and validated by micro-CT measurements (solid markers). Scale bars: 0.5 mm.

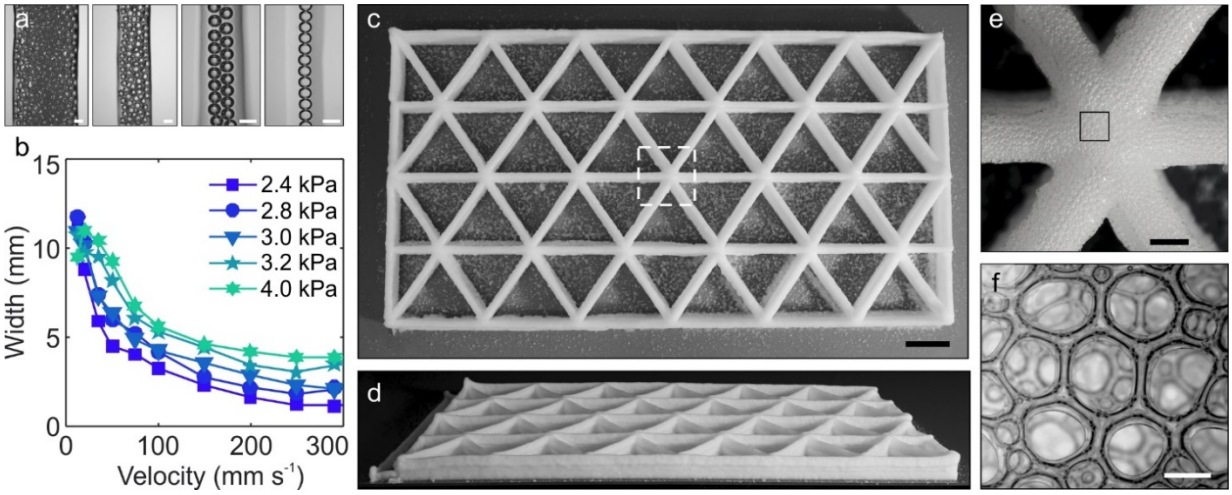

Figure 3: Direct bubble writing of hierarchical polymer foams. (a) Printed filaments formed by laterally moving the nozzle operated at P = 2.4 kPa for velocities of 35 mm s^{-1}, 70 mm s^{-1}, 150 mm s^{-1}, and 250 mm s^{-1} (left to right). (b) Filament width as a function of the printhead velocity and the gas pressure. (c,d) Large-scale 3D honeycomb, that was printed at a pressure of 4 kPa with a velocity of 60 mm s^{-1}. (e) View of the star-shaped strut connections, with (f) detail highlighting the small-scale cell architecture. Scale bars: (a) 1 mm; (c) 50 mm, (e) 5 mm, (f) 0.5 mm.

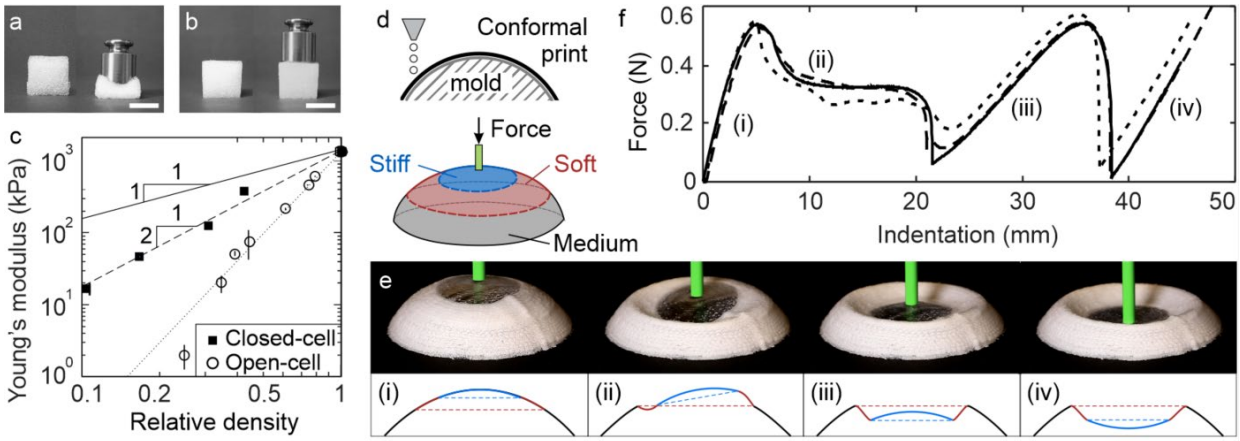

Figure 4: Mechanical properties of printed polymer foams. Optical images of (a) a soft foam with a Young's modulus of 10 kPa that strongly deforms upon compression by a 100-g load and (b) a stiff foam with a Young's modulus of 400 kPa that maintains its shape under the same load. (c) Log-log plot of Young's modulus as a function of the relative density for open- and closed-cell polymer foams. Theory predicts a power law exponent between 1 (solid line) and 2 (dashed line) for closed-cell materials and 2 for open-cell materials. The dotted line (with slope 4) indicates the slope of the open-cell data. (d) A spherical cap with sections of different stiffness was conformally printed onto a mold. (e) Images of the spherical cap during compression. The stiff top of this solid (bubble-free) cap is transparent. Bottom row: Schemes of different states obtained during translation. (f) Applied force as a function of indentation, in which the solid, dashed, and dotted lines indicate runs 1, 2, and 3, respectively. The numbers (i) to (iv) correspond to (e). Scale bars: 20 mm.

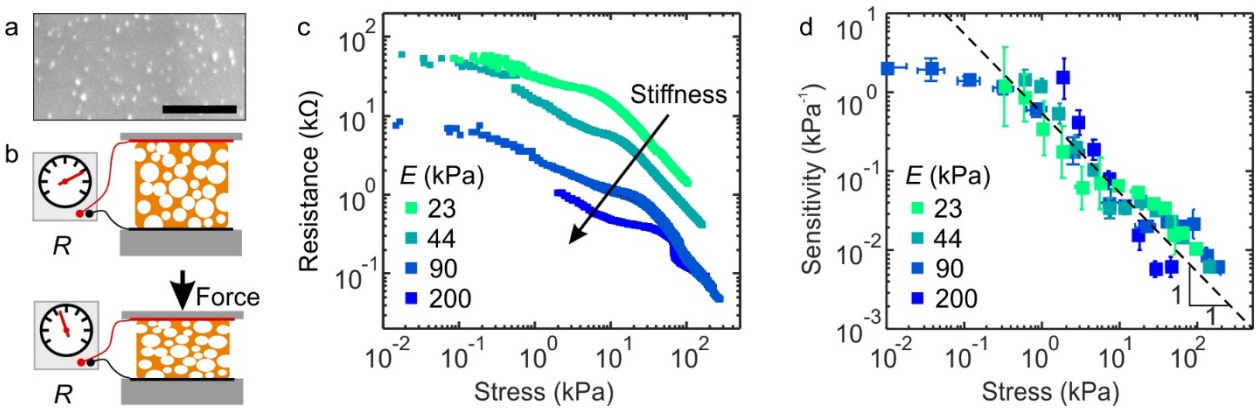

Figure 5: Conductive composite foams. (a) Optical image of the top surface of a representative conductive composite foam. Scale bar: 500 nm. (b) Schematic illustrations of composite foam compression between two electrodes, in which electric resistance is measured as a function of applied load. (c) Log-log plot of the electric resistance as a function of applied stress for conductive composite foams of different elastic moduli. (d) Log-log plot of sensitivity as a function of the applied stress, which reveals that these conductive composite foams may be used as pressure sensors that exhibit universal behavior independent of their stiffness.

References

[1] N. J. Mills, C. Fitzgerald, A. Gilchrist, R. Verdejo, *Compos. Sci. Technol.* **2003**, *63*, 2389.

[2] H. Bin Yao, J. Ge, C. F. Wang, X. Wang, W. Hu, Z. J. Zheng, Y. Ni, S. H. Yu, *Adv. Mater.* **2013**, *25*, 6692.

[3] B. Wicklein, A. Kocjan, G. Salazar-Alvarez, F. Carosio, G. Camino, M. Antonietti, L. Bergström, *Nat. Nanotechnol.* **2015**, *10*, 277.

[4] J. G. Gwon, S. K. Kim, J. H. Kim, *Mater. Des.* **2016**, *89*, 448.

[5] C. C. Wang, K. C. Yang, K. H. Lin, H. C. Liu, F. H. Lin, *Biomaterials* **2011**, *32*, 7118.

[6] L. J. Gibson, M. F. Ashby, *Proc. R. Soc. A Math. Phys. Eng. Sci.* **1982**, *382*, 43.

[7] L. J. Gibson, M. F. Ashby, *Cellular Solids: Structure and Properties*, Cambridge University Press, Cambridge, United Kingdom, **1999**.

[8] M. Szycher, *Szycher's Handbook of Polyurethanes*, CRC Press, Boca Raton, FL, USA, **2013**.

[9] K. J. Saunders, *Organic Polymer Chemistry*, Springer Science+Business Media, Dordrecht, The Netherlands, **1973**.

[10] J. E. Martini-Vvedensky, N. P. Suh, F. A. Waldman, *Microcellular Process for Closed Cell Foams and Their Method of Manufacture*, **1984**, 4473665.

[11] L. J. M. Jacobs, M. F. Kemmere, J. T. F. Keurentjes, *Green Chem.* **2008**, *10*, 731.

[12] M. S. Silverstein, *Prog. Polym. Sci.* **2014**, *39*, 199.

[13] D. Wu, F. Xu, B. Sun, R. Fu, H. He, K. Matyjaszewski, *Chem. Rev.* **2012**, *112*, 3959.

[14] A. R. Studart, U. T. Gonzenbach, E. Tervoort, L. J. Gauckler, *J. Am. Ceram. Soc.* **2006**, *89*, 1771.

[15] J. T. Muth, P. G. Dixon, L. Woish, L. J. Gibson, J. A. Lewis, *Proc. Natl. Acad. Sci.* **2017**, 201616769.

[16] B. E. Obi, *Polymeric Foams Structure - Property - Performance.*, Matthew Deans, Oxford, United Kingdom, **2018**.

[17] A. Testouri, L. R. Arriaga, C. Honorez, M. Ranft, J. Rodrigues, A. van der Net, A. Lecchi, A. Salonen, E. Rio, R. M. Guillermic, D. Langevin, W. Drenckhan, *Colloids Surfaces A Physicochem. Eng. Asp.* **2012**, *413*, 17.

[18] A. Testouri, M. Ranft, C. Honorez, N. Kaabeche, J. Ferbitz, D. Freidank, W. Drenckhan, *Adv. Eng. Mater.* **2013**, *15*, 1086.

[19] A. Quell, B. De Bergolis, W. Drenckhan, C. Stubenrauch, *Macromolecules* **2016**, *49*, 5059.

[20] J. Elsing, A. Quell, C. Stubenrauch, *Adv. Eng. Mater.* **2017**, *19*, 1700195.

[21] M. Costantini, J. Jaroszewicz, Ł. Kozon, K. Szlazak, S. Wojciech, P. Garstecki, C. Stubenrauch, A. Barbetta, J. Guzowski, *Angew. Chemie* **2019**, *58*, 7620.

[22] L. R. Meza, A. J. Zelhofer, N. Clarke, A. J. Mateos, D. M. Kochmann, J. R. Greer, *Proc. Natl. Acad. Sci.* **2015**, *112*, 11502.

[23] J. A. Lewis, *Adv. Funct. Mater.* **2006**, *16*, 2193.

[24] T. A. Schaedler, A. J. Jacobsen, A. Torrents, A. E. Sorensen, J. Lian, J. R. Greer, L. Valdevit, W. B. Carter, *Science (80-.).* **2011**, *334*, 962.

[25] X. Zheng, H. Lee, T. H. Weisgraber, M. Shusteff, J. DeOtte, E. B. Duoss, J. D. Kuntz, M. M. Biener, Q. Ge, J. A. Jackson, S. O. Kucheyev, N. X. Fang, C. M. Spadaccini, *Science (80-.).* **2014**, *344*, 1373.

[26] L. R. Meza, S. Das, J. R. Greer, *Science (80-.).* **2014**, *345*, 1322.

[27] M. F. Ashby, A. G. Evans, N. A. Fleck, L. J. Gibson, J. W. Hutchinson, H. N. G. Wadley, *Metal Foams: A Design Guide*, Butterworth-Heinemann, Burlington, MA, USA, **2000**.

[28] V. S. Deshpande, N. A. Fleck, M. F. Ashby, *J. Mech. Phys. Solids* **2001**, *49*, 1747.

[29] J. Mueller, K. Shea, *Extrem. Mech. Lett.* **2018**, *25*, 7.

[30] J. Mueller, J. R. Raney, K. Shea, J. A. Lewis, *Adv. Mater.* **2018**, *30*, 1705001.

[31] M. Y. He, V. S. Deshpande, J. W. Hutchinson, A. J. Jacobsen, W. Barvosa-Carter, *Int. J. Impact Eng.* **2010**, *37*, 947.

[32] D. T. Queheillalt, H. N. G. Wadley, *Acta Mater.* **2005**, *53*, 303.

[33] Q. Chen, P. F. Cao, R. C. Advincula, *Adv. Funct. Mater.* **2018**, *1800631*, 1.

[34] J. T. Muth, J. A. Lewis, *Langmuir* **2017**, *33*, 6869.

[35] C. Minas, D. Carnelli, E. Tervoort, A. R. Studart, *Adv. Mater.* **2016**, *28*, 9993.

[36] M. Sušec, S. C. Ligon, J. Stampfl, R. Liska, P. Krajnc, *Macromol. Rapid Commun.* **2013**, *34*, 938.

[37] X. Mu, T. Bertron, C. Dunn, H. Qiao, J. Wu, Z. Zhao, C. Saldana, H. J. Qi, *Mater. Horizons* **2017**, *4*, 442.

[38] S. C. Cox, J. A. Thornby, G. J. Gibbons, M. A. Williams, K. K. Mallick, *Mater. Sci. Eng. C* **2015**, *47*, 237.

[39] S. Andrieux, A. Quell, C. Stubenrauch, W. Drenckhan, *Adv. Colloid Interface Sci.* **2018**, *256*, 276.

[40] M. Naebe, K. Shirvanimoghaddam, *Appl. Mater. Today* **2016**, *5*, 223.

[41] L. Cui, M. A. Forero Rueda, M. D. Gilchrist, *Mater. Des.* **2009**, *30*, 3414.

[42] P. M. Biesheuvel, V. Breedveld, A. P. Higler, H. Verweij, *Chem. Eng. Sci.* **2001**, *56*, 3517.

[43] J. M. Kendall, *Phys. Fluids* **1986**, *29*, 2086.

[44] B. Louis, L. Lebel, B. Aissa, M. Ali, E. Khakani, D. Therriault, *Adv. Mater.* **2010**, *22*, 592.

[45] C. Clanet, J. C. Lasheras, *J. Fluid Mech.* **1999**, *383*, 307.

[46] H. Lhuissier, E. Villermaux, *J. Fluid Mech.* **2011**, *696*, 5.

[47] R. T. Ferrell, D. M. Himmelblau, *J. Chem. Eng. Data* **1967**, *12*, 111.

[48] E. Rio, A. L. Biance, *ChemPhysChem* **2014**, *15*, 3692.

[49] L. Hirt, A. Reiser, R. Spolenak, T. Zambelli, *Adv. Mater.* **2017**, *29*, 1604211.

[50] A. E. Simone, L. J. Gibson, *Acta Metall.* **1998**, *46*, 2139.

[51] E. Fantino, A. Chiappone, I. Roppolo, D. Manfredi, R. Bongiovanni, C. F. Pirri, F. Calignano, *Adv. Mater.* **2016**, *28*, 3712.

[52] J. Luo, R. Pohl, L. Qi, G. Römer, C. Sun, D. Lohse, C. W. Visser, *Small* **2017**, *13*, 1602553.

[53] L. L. Lebel, B. Aissa, M. A. El Khakani, D. Therriault, *Adv. Mater.* **2010**, *22*, 592.

Supporting Information

Supporting Information is available from the Wiley Online Library or from the author.

Acknowledgements

The authors gratefully thank Lorna Gibson (MIT) for useful discussions, Stefano Coco for experimental support, Lori Sanders for assistance with photo- and videography, and Alex Chortos for useful input regarding the foam-based pressure sensors. C.W.V. was sponsored by the Rubicon program of the Netherlands Organization for Scientific research (NWO). D.N.A acknowledges traineeship support from the NSF NRT program “Interface” (Award 1449999) through the University of Southern Mississippi. This research was funded by The Office of Naval Research Vannevar Bush Faculty Fellowship program under award number N000141612823. This work was performed in part at the Center for Nanoscale Systems (CNS), a member of the National Nanotechnology Coordinated Infrastructure Network (NNCI), which is supported by the National Science Foundation under NSF Award no. 1541959.

Competing interests

C.W.V. has co-founded IamFluidics B.V., which focuses on microparticle fabrication. J.A.L. has co-founded Voxel8, Inc, which focuses on 3D printing of functional materials.